






Experimental study of a helical acoustic streaming flowBjarne Vincent ^{1,2,*}, Sophie Miralles ^{1,†}, Daniel Henry ¹, Valéry Botton ¹,
and Alban Pothérat ²¹*Université de Lyon, INSA Lyon, CNRS, Ecole Centrale de Lyon, Université Claude Bernard Lyon 1,
Laboratoire de Mécanique des Fluides et d'Acoustique, UMR5509, 69621 Villeurbanne, France*²*Fluid and Complex Systems Research Centre, Coventry University, Coventry CV15FB, United Kingdom*

(Received 22 September 2023; accepted 1 February 2024; published 29 February 2024)

This paper presents an experimental investigation of a three-dimensional flow driven by acoustic forcing in a closed cavity. This problem is a generic model for streaming flows due to waves attenuating in fluids and reflecting on domain boundaries (for examples acoustic streaming in industrial processes but also streaming of gravity waves in geophysical context). The purpose of this work is to go beyond the current state of knowledge that is mostly limited to individual streaming jets and to characterize the flow obtained when the waves reflect on boundaries as it may occur in more realistic problems. To this end, we set up an experiment where we fire an ultrasonic beam radiated by a planar circular source so that it undergoes multiple reflections inside a water-filled cuboid cavity. This produces a helix-shaped acoustic field that drives the flow. The velocity field of the resulting three-dimensional flow is measured by means of particle tracking velocimetry (PTV) for different forcing magnitudes. The time-averaged fields obtained in the entire fluid domain feature jets following the acoustic beam and impinging the vertical boundaries of the cavity, giving rise to large vortical structures which are favorable for stirring purposes. Such acoustic field also generates fluid flows in both up and down directions, as well as an overall rotating motion for which an analytical scaling law is derived. Time-resolved PTV measurements in the vicinity of the first jet impingement shed light on the progressive development of unsteadiness with increasing forcing. The highly three-dimensional nature of the fluid motion and its observed dynamics make this flow particularly relevant for stirring applications at large scale.

DOI: [10.1103/PhysRevFluids.9.024101](https://doi.org/10.1103/PhysRevFluids.9.024101)**I. INTRODUCTION**

This paper seeks to experimentally characterize the properties and topology of flows driven by acoustic waves in a configuration where the reflection of sound on solid walls produces a three-dimensional force and a three-dimensional flow. Altering the geometry of the acoustic forcing by taking advantage of sound reflections on solid walls indeed vastly extends the range of flows that can be driven acoustically but calls for a better understanding of their properties.

While the first observations of acoustic streaming date back to the 19th century [1], the contactless character of acoustic forcing has been arising considerable interest much more recently in applications where flow control by more conventional means (for example mechanical) may be problematic. Notably, the development of small-scale fluid mechanics and microfluidics, where mechanical access is difficult, sparked a recent wave of interest in the contactless actuation of

*bjarne.vincent@insa-lyon.fr

†sophie.miralles@insa-lyon.fr

flows at small (submillimetric) scale [2–10]. There the pioneering works of Eckart, Westervelt, Nyborg, Lighthill, and coauthors [11–14] on the fundamentals of acoustic streaming found direct applications to various forms of “acoustic tweezers”: These indeed offer contactless tools to rotate, translate, mix, or oscillate very small quantities of fluids or droplets in highly confined geometries such as microchannels.

At a larger scale, contactless actuation offers a convenient way to handle fluids sensitive to external contamination or whose temperature or chemical reactivity renders mechanical actuation problematic. Such situations commonly occur in metallurgy where the casting of alloys requires adequate stirring to control the homogeneity and properties of the final solidified product. For example, the ability of acoustic streaming to induce contactless stirring [15] in a decimetric cavity is of potential interest to separate chemical species or to grow crystals from a melt [16]. In these processes, relatively slow flows are expected to have dramatic effect on the heat and mass transfers at the solid-liquid interface [17–22]. Compared to other possible actuation techniques, introducing an ultrasound beam in a liquid bath within a furnace can indeed be far less intrusive than using a propeller [23,24] or even electromotive forces necessitating cumbersome electromagnets, as often considered [25–28]. Similarly, a well-designed ultrasonic field may help controlling detrimental natural convection instabilities occurring in such processes [17,29,30].

In all these examples, the successful utilization of acoustic streaming demands the flexibility of adapting the topology of the forcing and its scale and intensity to the application at stake. This, in turn, requires an understanding at a fundamental level of how the geometry and intensity of the acoustic field translates into the properties of the flow it drives. In this respect, there are two very distinct types of streaming in these applications. The first type results in a force at short range from the actuator: It is implemented with ultrasonic actuators operating at relatively low frequencies and high powers typically hundreds of kilohertz and watts. It is widely used for the purpose of improving metallic blend solidification processes [31,32]. This approach relies on the creation of a cavitation cloud near the tip of the actuator to locally increase sound attenuation which, by promoting the conversion of acoustic energy into steady momentum over a short distance, gives rise to strong flows similar to free jets [33]. The coherence of the acoustic beam is thus lost at a quite small distance from the actuator. This makes it more difficult to adapt the acoustic force over a significant part of the domain.

For this reason, we are interested in streaming of the second type for the purpose of this paper. Here actuators operate at higher frequencies and lower powers and induce the so-called *Eckart* type of streaming in a homogeneous liquid without producing any cavitation [11]. The ultrasonic beam is then coherent over longer distances, which makes it possible to force flows far from the actuator [34–36], potentially over decimetric distances consistent with the sound attenuation length in common liquids. The long range is key in offering a much wider range of possibilities to alter the topology of the forcing. Indeed, in a cavity with dimensions comparable to this distance and containing a liquid, acoustic reflections on the walls can significantly increase the geometrical complexity of the acoustic field and, hence, of the forcing [37–39]. This has also been observed in sessile droplets of millimetric dimensions with 20-MHz ultrasounds in which acoustic reflections occurred at the drop free surface [40].

The question of characterizing the flow obtained by long-range streaming in fact reaches out well beyond the confines of acoustic streaming. Long-range streaming indeed also occurs for other types of waves. For example, internal gravity waves play a key role in geophysical flows where they are responsible for the occurrence of localized beams in atmosphere and oceans. The streaming they induce leads to the occurrence of nontrivial mean flows [41]. Localized laser beams can also induce streaming. Even though the mechanism may involve the mediation of an ultrasonic wave or scattering particles, photoacoustics, or particulate flows offer further possibility to alter the end-force acting on the flow [42–44]. These phenomena occur at vastly different lengthscales but they, too, call for a better understanding of the relation between the topology of the wave field, the applied force, and the resulting flow, in particular where boundaries are involved.

Whether streaming is used for the purpose of mixing or studied for its role in promoting turbulence, the questions are, first, to determine the flow structure: Is it two-dimensional (2D) or 3D? Planar or three-component? Steady or unsteady? What are the conditions of its stability [29], whether it is prone chaos and through which route [39]? For practical applications, the question is also whether walls reflect beams effectively enough to drive the flow over the entire volume of the cavity where the process of interest takes place (solidification, crystal growth, etc.). Answering these questions in detail would require application-specific studies but the basic mechanisms are best discovered in a simple geometry. Hence, we chose the simplest configuration with wall enclosing an entire volume: a parallelepipedic volume with a single incident beam, angled so as to undergo multiple reflections.

We choose to focus on the flow topology and scaling with the forcing and to answer these questions experimentally, using water as a working fluid so as to be able to map the flow by means of optical methods. Stability and transition to chaos are significantly more difficult to investigate experimentally because of the challenge of maintaining a steady forcing over extended periods of time [39]. More specifically, we study a three-dimensional acoustic streaming flow using particle tracking velocimetry (PTV). Our approach is to rely on successive reflections on the boundaries of the fluid domain to produce a complex-enough flow. The acoustic forcing is therefore 3D without any symmetries, promoting effective stirring properties. The considered vessel is nearly cubic, with a square base of $183 \times 183 \text{ mm}^2$; this size actually corresponds to the so-called G1 configuration in directional solidification photovoltaic silicon crucibles the smallest size for these processes. The acoustic beam is introduced into the vessel at a 45° horizontal angle with the side walls and a small vertical inclination so that the forcing points downwards and takes a nearly helical shape. We stress here that our purpose is not to optimize the stirring configuration for this specific cavity, which is generic, but rather to check that this original acoustic forcing is able to induce an overall global swirling flow in the whole fluid domain. Due to mass conservation, the induced descending flow along the helical forcing gives rise to ascending streams. Hence we expect a 3D three-components flow. It is, however, difficult to guess whether the return flow will mainly occur in the corners of the cavity or in its central region. This is an important issue since improving convective transport in the corners may be critical from the process standpoint in which stagnation areas must be avoided. This shall be one of the more specific questions regarding the flow topology that our study shall aim to address.

The paper is laid out as follows: First, the experimental setup and methodology considered to measure three-dimensional acoustic streaming flows are described (Sec. II). Section III is devoted to the description and analysis of the resulting jetlike structures and time-averaged large-scale helicity. The large-scale vertical and horizontal streams, and their dependency on the forcing magnitude, are analyzed in Sec. IV. We then focus on the flow structure near the first jet impingement, as well as its associated unsteadiness, which are discussed in Sec. V.

II. EXPERIMENTAL SETUP

A. Test rig and experimental methods

The considered setup, shown in Fig. 1, constitutes an evolution of the Acoustic STreaming Investigation Device (ASTRID) system [36,45]. The volume of investigation (VOI, $183 \times 183 \times 160 \text{ mm}^3$) is inside an aquarium made of glass. A glass plate featuring a hole covered by a plastic film in its upper half splits the aquarium into two separate impermeable volumes, both filled with water. The upper surface of the VOI is free.

The ultrasonic source, a plane circular transducer (IMASONIC) of active diameter $D_s = 30 \text{ mm}$, is placed outside the VOI. It operates at a constant electrical power P_{elec} ranging from 1 to 8 W and at a fixed frequency of 2 MHz and generates beam-shaped acoustic fields [36]. The highly directional nature of the beam is exploited to create a more intricate configuration by giving the transducer a horizontal tilt angle of 45° and a vertical inclination $\gamma = 8^\circ$. The vertical inclination

TABLE I. Hardware and recording parameters used for PTV flow measurements in the entire fluid domain (first setup, left column) and near the first jet impingement (second setup, right column).

	Overall time-averaged flow measurements	Near-impingement flow measurements
Size of the measurement domain	$179 \times 179 \times 160 \text{ mm}^3$ (length \times width \times height) cuboid.	Elliptic cross section, approximately $170 \times 25 \times 75 \text{ mm}^3$. (length \times width \times height).
Light source	<i>LaVision GmbH</i> LED Flashlight 300 (blue), pulsed-overdrive mode, pulse duration: 335 μs . LED panel is placed at approximately 5 cm from the VOI.	Double cavity Nd:Yag pulsed laser (wavelength: 532 nm). The light beam is expanded using the Compact Volume Optics device by <i>LaVision GmbH</i> fitted with a cylindrical lense (focal length of -150 mm) and placed at 32 cm from the VOI.
Focal length of the camera lenses	12 mm	25 mm
Optical filters	None	High-pass Kodak Wratten 22 (cutoff wavelength: $\approx 550 \text{ nm}$)
Seeding particles	<i>Dantec Dynamics</i> polyamid seeding particles (PSP), 5 μm in diameter, density of 1030 kg/m^3 .	<i>microParticles GmbH</i> fluorescent polystyrene particles (PS-FluoRed-5.0), 5 μm in diameter, density of 1050 kg/m^3 .
Frame rate	4 Hz (1 W), 8 Hz (2 and 4 W) and 16 Hz (6 and 8 W)	1.875 Hz (1 W), 2.5 Hz (2 W) and 5 Hz (4, 6, and 8 W).
Exposure	335 μs	105 μs
Recording duration	12.5 min (1 W), 20.8 min (2, 4, 6, and 8 W).	20.0 min (all powers).

The velocity fields are measured by PTV: seeding particles are tracked inside the fluid volume, and their trajectories are determined using the “Shake-The-Box” algorithm [47]. The corresponding Eulerian velocity fields are then reconstructed using a “binning” method applied at each time step. The averaging procedure involves a Gaussian weight based on the distance between the instantaneous particle track position and the center of the cell where the Eulerian velocity vector is determined.

The PTV measurements of the velocity fields are carried out using hardware manufactured by LaVision GmbH. The images are recorded using their MiniShaker device, which features four 10-bit cameras (Basler acA1920-150um CMOS sensors), each pointing towards the center of the measurement volume. The frames are then processed with the DaVis 10 software. The seeding particles are typically 5 μm in diameter, i.e., they are sufficiently small to prevent the deterioration of their tracking ability due to the acoustic radiation pressure [48]. While mean velocity vector fields $\bar{\mathbf{u}}$ (the symbol $\bar{}$ refers to time average over the recording duration) could be determined in almost the whole VOI, the measurement domain was significantly reduced in a second light setup to capture the flow unsteadiness near the beam reflection point A (green-shaded zone in Fig. 1). This region is lit by expanding a laser beam into a volume of elliptic transverse cross section. Detailed setup, as well as recording parameters, are given in Table I. For both light setups, at least 20 min separate two consecutive recordings carried out at different acoustic forcing magnitudes in order to avoid the measurement of any transient state. Grid resolutions $\Delta x = 2.2$ and 1.4 mm are obtained for the mean and time-resolved measurements, respectively.

Measurements are poor near glass walls because of light reflections, so the domain is slightly cropped in both horizontal directions to avoid spurious data there (x and z range from -89.5 to 89.5 mm). Note that this issue is overcome for the time-resolved measurements using a monochro-

TABLE II. Typical properties of the fluid samples used in the present study [50]. Fluid is water at $T = 20^\circ\text{C}$ and atmospheric pressure, and $f = 2\text{MHz}$.

ρ (kg/m ³)	ν (m ² /s)	c (m/s)	η (Pa s)	2α (m ⁻¹)
998.2	1.004×10^{-6}	1483	3.006×10^{-3}	0.211

matic light source in conjunction with fluorescent particles. The wavelength of the light emitted by the particles can be isolated with filters, which reduce the captured light intensity. Hence, this approach was dedicated to measurements in small volumes where laser light could be more focused.

To assess the sensitivity of the mean fields with the number of frames used in the time-averaging process, the discrepancy between the values of $\|\bar{\mathbf{u}}\|$ computed using either 75% or 100% of the total recording duration was quantified at several points in the VOI. For instance, at $(x, y, z) = (0, 10, 75)\text{mm}$ and $(0, 10, -75)\text{mm}$ (i.e., two opposite points on the optical path of the cameras), the measured discrepancies on $\|\bar{\mathbf{u}}\|$ are typically about 3% and 1.5%, respectively, confirming that converged mean fields are obtained over the recording durations listed in Table I.

Finally, the experimental setup and methodology have been benchmarked against a former experimental work using PIV [38]. The mean discrepancy on the longitudinal profiles of jet velocity magnitude measured by PIV and PTV is less than 11.2%. Considering that these methods were not operated simultaneously, the agreement between the results obtained using either methodology, as well as the additional ability of PTV to recover three-dimensional data, highlights the suitability of this approach to investigate acoustic streaming flows at decimetric scales.

B. Control parameter

Using the test rig and procedures described in Sec. II A, three-dimensional velocity fields have been measured for values of P_{elec} equal to 1, 2, 4, 6, or 8 W, while keeping the other parameters constant. The electrical power is related to its acoustic counterpart P_{ac} through the transducer efficiency ε :

$$P_{\text{ac}} = \varepsilon P_{\text{elec}},$$

with ε ranging from 76.1% for $P_{\text{elec}} = 1.6\text{ W}$ to 78.6% for $P_{\text{elec}} = 8.2\text{ W}$ [49].

The control parameter P_{elec} can be further expressed by means of the acoustic Grashof number Gr_{ac} , defined as the ratio between the acoustic forcing magnitude and viscous effects at the scale of the source [22]:

$$\text{Gr}_{\text{ac}} = \frac{32\alpha P_{\text{ac}} D_s}{\pi \rho c \nu^2}, \quad (1)$$

where ρ , ν , and c refer to the fluid density, its kinematic viscosity, and the speed of sound, respectively. If acoustic dissipation is mostly due to viscous effects, as it is the case for water [36], then the acoustic power absorption coefficient 2α is

$$2\alpha = \frac{4\pi^2 f^2}{\rho c^3} \left(\frac{4}{3} \mu + \eta \right),$$

where $\mu = \rho \nu$, f , and η refer to the dynamic viscosity, the sound frequency, and the bulk viscosity, respectively. The typical values of these parameters are listed in Table II.

The amount of dissipated acoustic power can be quantified by the dimensionless number $2N = 2\alpha L_{\text{helix}}$ [36], which compares L_{helix} to the characteristic acoustic power dissipation length $1/(2\alpha)$. With $2N \approx 0.15$ in the present case, the loss of acoustic energy (hence drop of forcing magnitude) is about 14% along the beam axis.

TABLE III. Conversion table between the electrical power P_{elec} and acoustic Grashof number Gr_{ac} . Values of the acoustic source efficiency ε are obtained through linear interpolation of tabulated data provided by the transducer manufacturer IMASONIC [49]. Temperatures are given at the start and the end of each recording. Values of Gr_{ac} are bounded using Eq. (2), where ΔT is estimated as the sum of twice the thermometer resolution (0.25 °C) and the temperature difference between the beginning and the end of each recording. The derivatives in Eq. (2) have been estimated by fitting cubic curves to reference tables [50].

P_{elec} (W)	ε (%)	Overall mean flow measurements		Near-impingement measurements	
		Temp. (°C)	Gr_{ac}	Temp. (°C)	Gr_{ac}
1	75.0	[26.0, 26.0]	$(1.78 \pm 0.03) \times 10^4$	[21.5, 21.5]	$(1.65 \pm 0.03) \times 10^4$
2	76.6	[26.0, 26.0]	$(3.64 \pm 0.05) \times 10^4$	[21.0, 21.5]	$(3.37 \pm 0.11) \times 10^4$
4	78.7	[26.0, 26.5]	$(7.50 \pm 0.22) \times 10^4$	[20.0, 20.5]	$(6.82 \pm 0.23) \times 10^4$
6	78.6	[26.5, 26.5]	$(11.28 \pm 0.17) \times 10^4$	[20.5, 21.0]	$(10.29 \pm 0.34) \times 10^4$
8	78.8	[26.5, 27.0]	$(15.12 \pm 0.44) \times 10^4$	[21.0, 21.0]	$(13.80 \pm 0.23) \times 10^4$

Care has been taken to account for variations of material properties caused by small temperature departures. Assuming that $\eta \approx 3\mu$ for water [36], the absolute uncertainty on Gr_{ac} is

$$\Delta \text{Gr}_{\text{ac}} = \text{Gr}_{\text{ac}} \left(\frac{1}{\rho} \left| \frac{d\rho}{dT} \right| + \frac{1}{\nu} \left| \frac{d\nu}{dT} \right| + \frac{4}{c} \left| \frac{dc}{dT} \right| \right) \Delta T. \quad (2)$$

Its corresponding values, obtained by fitting reference tables [50], are listed in Table III. For each measurement campaign, the temperature of water was measured before and after each recording. The temperature difference was typically about 0.5 °C, which, added to the temperature reading uncertainty due to the thermometer resolution, yields a maximum uncertainty of 3.3% on Gr_{ac} for the measurements made near the first jet impingement for $P_{\text{elec}} = 4$ W. The sensitivity of Gr_{ac} to temperature was further observed by comparing values obtained at the same electrical power but at different temperatures, for the overall time-averaged flow and near-impingement measurements. For instance, the discrepancy reaches 10% for $P_{\text{elec}} = 4$ W (Table III). From next section, all the results are given with nondimensional quantities where D_s , D_s^2/ν , and ρD_s^3 are taken as length, time, and mass scales, respectively.

III. MAIN STRUCTURES OF TIME-AVERAGED HELICAL FLOW

Over the range of parameters investigated, the flow was found either steady or unsteady. The time-averaged flow resulting from the helix-shaped acoustic force field introduced in the cavity displays a highly three-dimensional nature, and despite the different forcing magnitudes, share qualitatively similar features. These features therefore appear robust and, as such, illustrate well the basic properties of flow driven acoustically through reflection in a cavity. We first describe the main jets sustained by the acoustic forcing, which forms the overall flow structure, then seek scaling laws for their intensity, which may be transposed to other problems. In a second subsection, another important feature of the flow is investigated, namely the helicity created by the impingements of the jets on the walls.

A. Jetlike structures at the scale of the acoustic forcing

The time-averaged flow features strong jets along the beam axis (Fig. 2 and see the animation in Ref. [51]), each impinging a vertical cavity wall and contributing to an overall rotating fluid motion about a vertical axis. Similarly to what has been observed in Refs. [37–39], the jets spread downstream each impingement and in both vertical directions, giving rise to large recirculating structures close to the cavity walls.

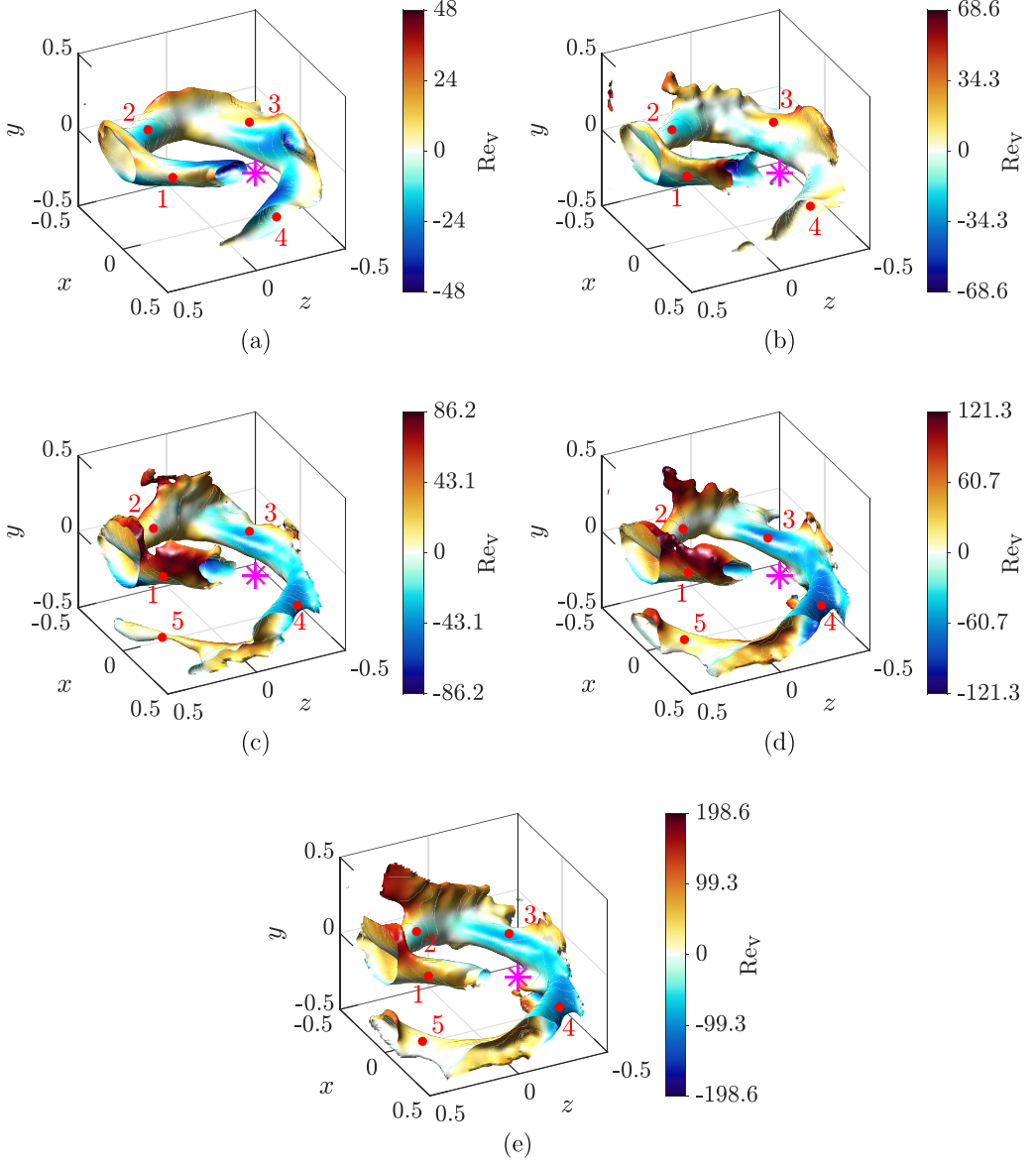


FIG. 2. Isocontours of velocity magnitude colored by the Reynolds number based on the vertical velocity for time-averaged flows measured at different values of acoustic Grashof numbers: (a) $Gr_{ac} = 1.78 \times 10^4$ ($P_{elec} = 1$ W), (b) 3.64×10^4 (2 W), (c) 7.50×10^4 (4 W), (d) 11.28×10^4 (6 W), and (e) 15.12×10^4 (8 W). Isocontours of velocity magnitude are plotted at 2.5, 3.2, 4.7, 6.2 and 7.7 mm/s, respectively, corresponding to $Re = 87.11, 111.51, 163.77, 216.04, 268.31$. The purple star at $(x, y, z) = (0.5, 0.13, 0)$ locates the entry point of the acoustic beam in the VOI. The spatial coordinates are normalized by the dimensions of the VOI (183 mm for the horizontal directions and 160 mm for the vertical one).

One can observe that, for increasing values of Gr_{ac} , the jets are more sharply defined, as in simpler configurations [38]. Four main jets are clearly visible for all investigated forcings. The emergence of a fifth jet with velocity levels similar to those of the other jets when Gr_{ac} is increased indicates an interaction between the rotating motion and the jet structures originating from the forcing. The jet

velocity magnitude levels depend on Gr_{ac} , and increasing the injected power enhances the inertia of each jet, resulting in their larger inertia-caused spreading at their impingements. For instance, these structures are particularly visible downstream impingements of jets 3 and 4 for $Gr_{ac} \geq 7.5 \times 10^4$ [Figs. 2(c), 2(d) and 2(e)] but are not observed for smaller powers.

In the case of a free jet driven by a straight beam in a large fluid domain, previous studies have shown that two regimes can be expected, depending on whether the acoustic force is balanced by inertia or viscous forces [36]. To be observed in the present case, the transition between the two regimes should occur at a distance x'_{tr} from the jet origin that is shorter than the jet length. Equating the two scaling laws derived in a one-dimensional approach for these regimes (Eqs. (19) and (22) in Ref. [36]) yields a relationship between x'_{tr} and Gr_{ac} which, assuming that the beam radius $R_{beam} \approx 1/2$, predicts a transition occurring at $x'_{tr} = 2.17$ (i.e., the half distance on the beam axis between two consecutive acoustic reflections, in nondimensional units) for $Gr_{ac} \approx 140$. As $Gr_{ac} > 10^4$ in the present case, the corresponding regime transition distance is significantly greater than the maximum jet length in the VOI; hence, no transition from the inertial to the viscous regime can be observed. The acoustic forcing is then essentially balanced by inertia in the observed jets, meaning that the velocity on each jet axis scales as $\sqrt{Gr_{ac}x'}$ (x' is the distance from the jet origin along its axis) [36,45]. As mentioned in Sec. II B, the acoustic forcing magnitude decreases along the beam due to sound attenuation. Accounting for this effect in the forcing parameter for each jet, a convenient Grashof number can be defined as $Gr'_{ac} = Gr_{ac}e^{-2\frac{N}{L_{ac}}x'_s}$, where x'_s is the distance on the beam axis to the acoustic source normalized by D_s and $L_{ac} = L_{helix}/D_s$. Thus, the velocity of the jets can be estimated by

$$Re_{jet} \approx K \sqrt{Gr'_{ac}x'}, \quad (3)$$

in which the Reynolds number Re_{jet} is based on the time-averaged jet velocity magnitude $\|\bar{\mathbf{u}}_{jet}\|$ and D_s , x' is the distance from the jet origin along its axis normalized by D_s and $K = 1/2$ for a straight free jet. In the present configuration, the jet axes have been determined by tracking the points of maximum velocity in successive planes cutting the jets. The straight line fitted to these points is considered as the jet axis, and the jet origin $x' = 0$ is defined as the intersection of the axis and the upstream vertical wall. Points near the impingements are deliberately left out of the procedure described above: The jet deformation due to the impact may give rise to local maximum velocity points located off the actual jet axis, hence preventing its determination. This methodology has been successfully applied to jets 1, 3, and 4 (Fig. 3). Jet 5 has been discarded from this analysis since it was observed for the highest values of Gr_{ac} only. Jet 2 has not been considered either for this analysis because its axis exhibited a too strong bending caused by the spreading of jet 5 (Fig. 2).

Close to the jet origin ($x' < 1$), jet 1 has a distinct behavior from the other jets (Fig. 3): The velocity magnitude profile on its axis features a steep increase for each forcing magnitude, which has already been observed in short jets [45] and is related to the fact that the origin of jet 1 corresponds to the entrance point of the beam in the VOI. In contrast, the origins of all the other jets lie in regions of fluid where a jet impingement occurs and important velocity magnitudes are encountered [37]. At distances sufficiently far downstream the jet origin, the velocity of these jets drops before increasing again smoothly until the next impingement point is reached. The scaling law given by Eq. (3) is valid in regions where the jets are free from effects of both the upstream and downstream impingements, i.e., approximately $2 \leq x' \leq 3.5$ in the present case. Scaling laws similar to Eq. (3) were sought for jets 1, 3, and 4 for different values of P_{elec} (hence Gr_{ac}) by determining the coefficient K in Eq. (3) using least-squares fitting. For each jet, the computed value of K is greater than the value for a straight jet ($K = 0.59, 0.72$, and 0.65 for jets 1, 3, and 4, respectively). However, the slopes of the resulting scaling laws do not differ significantly from their straight jet counterpart, despite the undeniable three-dimensionality of the flow. Finally, the scaling $Re_{jet}/\sqrt{Gr'_{ac}} \approx 1$ remains valid for each jet. This means that not only Eq. (3) yields appropriate estimates of the jet velocity magnitudes in this studied configuration, but it also indicates that, since the sound absorption is weak in the present case (as explained in Sec. II B), similar velocities are encountered in jets 1, 3, and 4 for

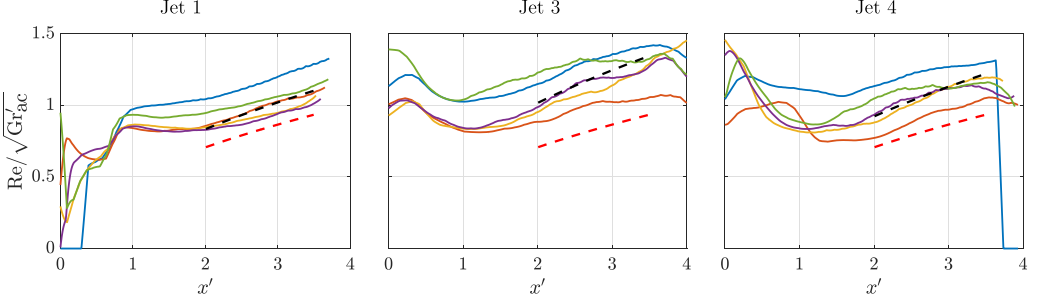


FIG. 3. Profiles of jets Reynolds numbers along the axis of jets 1, 3, and 4, and for all values of investigated power: $\text{Gr}_{\text{ac}} = 1.778 \times 10^4$ ($P_{\text{elec}} = 1$ W) in blue, $\text{Gr}_{\text{ac}} = 3.637 \times 10^4$ (2 W) in orange, $\text{Gr}_{\text{ac}} = 7.499 \times 10^4$ (4 W) in yellow, $\text{Gr}_{\text{ac}} = 11.28 \times 10^4$ (6 W) in purple, and $\text{Gr}_{\text{ac}} = 15.12 \times 10^4$ (8 W) in green. The distance from the estimated jet origin, normalized by the transducer diameter D_s , is designated by x' . The red dashed line represents the scaling law of a straight acoustic streaming jet [Eq. (3) with $K = 1/2$]. The black dashed line corresponds to a similar scaling law, with K being determined using least-squares fitting: $K = 0.59$ (jet 1), 0.72 (jet 3), and 0.65 (jet 4). Experimental data are fitted on the interval over which the black and red dashed lines are plotted. The same scale on the y axis is used for each figure.

a given forcing [typical values of $\|\bar{\mathbf{u}}_{\text{jet}}\|$ are about 4, 8 and 12 mm/s ($\text{Re} = 119, 239$ and 358) for $P_{\text{elec}} = 1, 4$ and 8 W ($\text{Gr}_{\text{ac}} = 1.78, 7.5$ and 15.12×10^4), respectively].

As a conclusion, although the studied flow displays highly three-dimensional features, the observed jets locally obey to the same scaling law as a single free jet driven by a straight beam. This confirms that these jet structures are similar to those encountered in formerly studied configurations [36,37,45]. This also suggests that a complex flow may be constructed “piecewise,” choosing reflection points to alter the geometry of the flow using these scaling laws to predict its intensity locally.

B. Helicity created by jet impingements

Due to the presence of solid boundaries, the overall time-averaged flow is more complex than the broken-line helix formed by the structure of the main jets. The impingement of the jets on the vertical wall creates strong local vorticity. The development of these structures may be more or less facilitated by the vicinity of another jet impinging the same surface but at a different y coordinate. For instance, the first impingement I_1 , defined as the point where the axis of jet 1 crosses the vertical wall downstream, interacts with I_5 on the same wall but at lower y coordinate (Fig. 2). This restricts the development of a large downward fluid motion below I_1 .

Coupling of these local recirculating motions near the impingements with the overall rotating motion yields large three-dimensional vortical structures, which are made clearly visible by the Q criterion [52,53] (Fig. 4(a) and see the animation in Ref. [54]). The rotation motion, combined with the creation of vorticity at the walls, generates helicity. The normalized helicity \tilde{h} coloring the isocontour in Fig. 4(a) is defined as

$$\tilde{h} = \frac{\bar{\mathbf{u}} \cdot \bar{\boldsymbol{\omega}}}{\|\bar{\mathbf{u}}\| \|\bar{\boldsymbol{\omega}}\|}, \quad (4)$$

where $\bar{\boldsymbol{\omega}}$ is the time-averaged vorticity. The sign of \tilde{h} can actually be determined beforehand; we shall consider the vortex above the impingement of jet 1 as an illustrative example. This vortex rotates about the horizontal x axis, so that $\bar{\boldsymbol{\omega}}$ points in the negative x direction there. Besides, the overall rotation sustained by the jets gives $\bar{\mathbf{u}} \cdot \bar{\mathbf{e}}_x < 0$ in that vortex (with $\bar{\mathbf{e}}_x$ the unit vector pointing in the positive x direction). From Eq. (4), \tilde{h} is thus positive. The same reasoning can actually be applied to any vortex located above an impingement (including those close to the

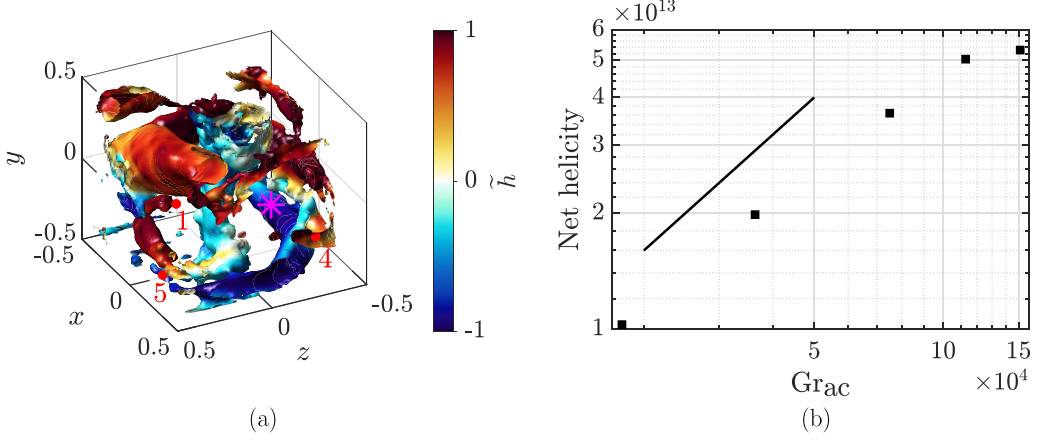


FIG. 4. (a) Isocontour of Q criterion (1.86×10^4 in nondimensional units) colored by the normalized helicity \tilde{h} , as defined by Eq. (4). The isocontour is shown for $Gr_{ac} = 15.12 \times 10^4$, with the location of the acoustic beam entry point in the VOI identified by a purple star at $(x, y, z) = (0.5, 0.13, 0)$. The red dots corresponds to the locations of the main jets. (b) Evolution with Gr_{ac} of the dimensionless net helicity, obtained by integrating $\|\bar{\mathbf{u}}\| \|\bar{\boldsymbol{\omega}}\| \tilde{h}$ over the cavity volume (data points lying too close to the boundaries are ignored, as well as those located near the free surface). The solid line represents an affine law.

free surface), since $\bar{\mathbf{u}}$ and $\bar{\boldsymbol{\omega}}$ are aligned in such structure. In contrast, a vortex beneath a jet impingement rotates in the opposite direction. This results in $\bar{\boldsymbol{\omega}}$ being locally opposed to $\bar{\mathbf{u}}$, which yields $\tilde{h} < 0$. An example illustrating this point is the vortex below I_3 . This vortex is stretched by the overall rotating motion, creating a large J-shaped structure of negative \tilde{h} near the bottom wall. Except this structure, the horizontal vortices of highest intensity mostly are located above the jets [Fig. 4(a)]. This is made visible by the duplication of the jet locations and numbering introduced in Fig. 2.

In addition to the horizontal vortices at the impingements, a large vertical vortex appears at the center of the cavity. On that isocontour, $\bar{\mathbf{u}}$ and $\bar{\boldsymbol{\omega}}$ are almost orthogonal, explaining the marginal local values of \tilde{h} . This region of uprising fluid, referred to as the “chimney” in the remaining of this document, is bounded by regions of downwards-flowing fluid driven by the jets.

Finally, the different vortical structures create a positive net helicity within the cavity [Fig. 4(b)]. This quantity increases linearly with Gr_{ac} for $Gr_{ac} \leq 11.28 \times 10^4$. At $Gr_{ac} = 15.12 \times 10^4$, a large contribution of the helicity close to the walls may be screened by the dimensions of the VOI, which are slightly smaller than the actual cavity. The net helicity may thus be underestimated at this forcing. Nevertheless, net helicity here essentially originates from horizontal vortices, despite the forcing field being shaped as a vertical helix.

The net helicity of this flow may be changed by increasing the forcing by modifying the helix pitch (not studied here) or by increasing the vertical dimension of the cavity. Tuning easily the helicity can be of interest for studying induction mechanisms in MHD flows or for atmospheric rotating flows like hurricanes.

IV. LARGE-SCALE SECONDARY FLOW: THREE-DIMENSIONALITY CHARACTERIZATION

Besides of the jets, the helical streaming flow features horizontal and vertical streams (in both ascending and descending directions). Knowing their intensity, and how that intensity varies with Gr_{ac} , may be of crucial importance in stirring applications for instance. For this reason, we shall

first study the evolution with Gr_{ac} of the swirling (i.e., rotation) motion magnitude. We shall then characterize the vertical streams.

A. Characterization of the time-averaged horizontal rotation

Just like the multiple jets studied in the previous sections, the swirling motion is one of the key features of the flow obtained by reflection that does not occur in single acoustic streaming jets. The velocity magnitude associated with the swirl may be quantified in each constant- y plane in which the rotating motion is observed (see the left panel of Fig. 6). In each constant- y plane, the center of rotation O' can be located to define a local polar coordinate system $(O', \mathbf{e}_r, \mathbf{e}_\theta)$, in which \mathbf{e}_r and \mathbf{e}_θ are the unit vectors in the radial and azimuthal directions, respectively. The time-averaged azimuthal velocity at a point M such as $O'M = r \mathbf{e}_r$ is then given by $\overline{u}_\theta = \overline{\mathbf{u}} \cdot \mathbf{e}_\theta$, which can be averaged over both θ and y coordinates to yield a single evaluation of $\overline{u}_\theta(r)$ per acoustic forcing:

$$\langle \overline{u}_\theta(r) \rangle_{\theta,y} = \frac{1}{N_\theta N_y} \sum_{j=1}^{N_y} \sum_{i=1}^{N_\theta} \overline{\mathbf{u}}(r, \theta_i, y_j) \cdot \mathbf{e}_\theta, \quad (5)$$

where $\langle \rangle_{\theta,y}$ refers to the ensemble averages over the N_θ azimuthal angles and N_y y coordinates. While N_θ can be the same for all Gr_{ac} , N_y greatly depends on the interval of y coordinates over which the overall rotating motion is observed. In the present work, N_y ranges between 47 for $\text{Gr}_{\text{ac}} = 3.637 \times 10^4$ and 68 for $\text{Gr}_{\text{ac}} \geq 7.50 \times 10^4$. For all Gr_{ac} , N_θ is set to 20 (greater values of N_θ yield an improvement of less than 1%). In total, at least 940 points are thus used to estimate $\langle \overline{u}_\theta(r) \rangle_{\theta,y}$.

The radial profiles of Re_θ , the Reynolds number based on Eq. (5), show an enhancement of the swirl motion as Gr_{ac} is increased [Fig. 5(a)]. For $\text{Gr}_{\text{ac}} \leq 3.64 \times 10^4$, this swirl is a solid-body rotation, with Re_θ scaling as $\text{Re}_\theta \propto \text{Gr}_{\text{ac}}^{1/2}$. Above $r/D_s \approx 2.5$, Re_θ drops because of the no-slip boundary condition imposed by the nearby vertical walls. For $\text{Gr}_{\text{ac}} \geq 7.50 \times 10^4$, the obtained profiles are different: They feature a nonlinear evolution with two regions over which Re_θ increases with r/D_s at different rates. The radial position where the change of slope occurs increases with the forcing. In contrast, the maximum Re_θ is consistently found at a distance $\delta/D_s \sim 0.5$ from the nearest wall, whatever the Gr_{ac} .

A single velocity estimate for the swirl motion can be obtained by further averaging the $\langle \overline{u}_\theta \rangle_{\theta,y}$ profiles over r [squares in Fig. 5(b)]. The evolution of this quantity with Gr_{ac} can be explained as follows: The jets, of time-averaged velocity $\overline{\mathbf{u}}_{\text{jet}}$, drive the swirl by viscous entrainment. Balancing the torque driven by the N_{jets} jets with the one resulting from the friction on the vertical walls yields:

$$N_{\text{jets}} \overbrace{\sigma_{\text{jet}} S_{\text{jet}}}^{\text{Friction on the lateral jet surface}} \underbrace{L_a}_{\text{Lever arm}} \sim N_{\text{jets}} \overbrace{\sigma_f S_f}^{\text{Wall friction}} \underbrace{\frac{L}{2}}_{\text{Lever arm}}, \quad (6)$$

where L is the cavity width, $L_a = L\sqrt{2}/4$, and σ_{jet} and σ_f are the viscous shear stresses on the lateral jet surface S_{jet} and on the wall friction surface S_f , respectively. Then, by assuming that the jet length L_{jet} is approximately equal to the horizontal distance between two consecutive acoustic reflection points, i.e., $L_{\text{jet}} \sim L/\sqrt{2}$:

$$\sigma_{\text{jet}} S_{\text{jet}} \sim \mu \frac{\|\overline{\mathbf{u}}_{\text{jet}}\|}{\frac{D_s}{2}} \pi D_s L_{\text{jet}} \sim \sqrt{2} \mu \pi L \|\overline{\mathbf{u}}_{\text{jet}}\|. \quad (7)$$

As the wall friction surface actually involved in the torque balance is expected to be smaller than the area of a single vertical wall, S_f is defined as $S_f \sim \beta H L$, where H is the cavity height and $\beta < 1$ is

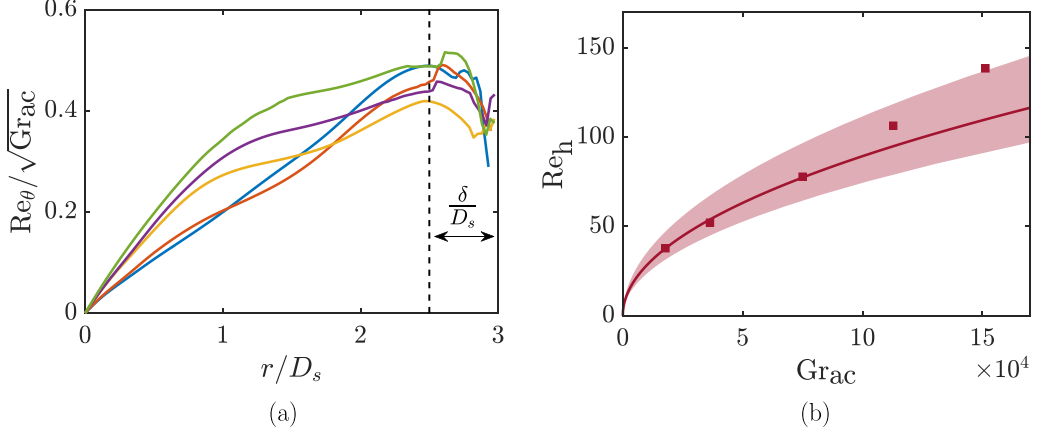


FIG. 5. (a) Radial profiles of the Reynolds number Re_θ based on the mean azimuthal velocity $\langle \bar{u}_\theta \rangle_{\theta,y}$ and D_s for different values of Gr_{ac} : $Gr_{ac} = 1.78 \times 10^4$ ($P_{elec} = 1$ W) in blue, $Gr_{ac} = 3.64 \times 10^4$ (2 W) in orange, $Gr_{ac} = 7.50 \times 10^4$ (4 W) in yellow, $Gr_{ac} = 11.28 \times 10^4$ (6 W) in purple, and $Gr_{ac} = 15.12 \times 10^4$ (8 W) in green. The profiles are computed using Eq. (5). The mean distance between the point of maximum velocity and the vertical walls is denoted by δ . (b) Evolution of Re_h with Gr_{ac} , where Re_h is the azimuthal Reynolds number averaged over the radial coordinates for each forcing magnitude: experimental points (squares) and prediction (red curve and area). The square-root dependency on the Grashof number is obtained using Eqs. (9) and (3) for $\beta = 0.5$, $\delta = 15$ mm, $L = 183$ mm, $K = 0.65$, and $x' = 2.2$, and the envelope (red area) is plotted for the same parameter values but for $\beta = 0.6$ (lower bound) and $\beta = 0.4$ (upper bound).

a tuning parameter. Since the velocity gradient length scale is δ at the wall [Fig. 5(a)]:

$$\sigma_f S_f \sim \mu \frac{2 \langle \bar{u}_\theta \rangle_{r,\theta,y}}{\delta} \beta H L, \quad (8)$$

where $\langle \bar{u}_\theta \rangle_{r,\theta,y}$ is the mean value of the radial profile of azimuthal velocity for a given forcing. Using Eqs. (7) and (8), the torque balance yields:

$$Re_h \sim \frac{\pi}{2\beta} \frac{\delta}{H} Re_{jet}, \quad (9)$$

where Re_h is the Reynolds number based on $\langle \bar{u}_\theta \rangle_{r,\theta,y}$ and is representative of the overall horizontal fluid flow. The jet Reynolds number is obtained by evaluating Eq. (3) at a relevant distance from the jet origin, which is typically $x' \approx L_{jet}/(2D_s)$ and introduces a square-root dependency of Re_h on Gr_{ac} , which is experimentally observed for $Gr_{ac} \leq 7.50 \times 10^4$. The discrepancy between the experimental points and the scaling law given by Eq. (9) however increases at higher power. This trend may be attributed to the development of flow unsteadiness as Gr_{ac} is increased, which is not accounted for in the derivation of Eq. (9).

B. Evolution of the vertical fluxes with power

In addition to the swirling motion studied above, the jets are also responsible for vertical flows in both the upward and downward directions. We shall now study these streams in more details and quantify their dependency on Gr_{ac} .

The helix-shaped forcing field induces a downward flow. This motion is sustained by the jets; it mainly occurs in the bulk of the flow and marginally beneath each jet impingement (Fig. 6). In constant- y planes, these regions of downward flow appear as large surfaces of negative vertical

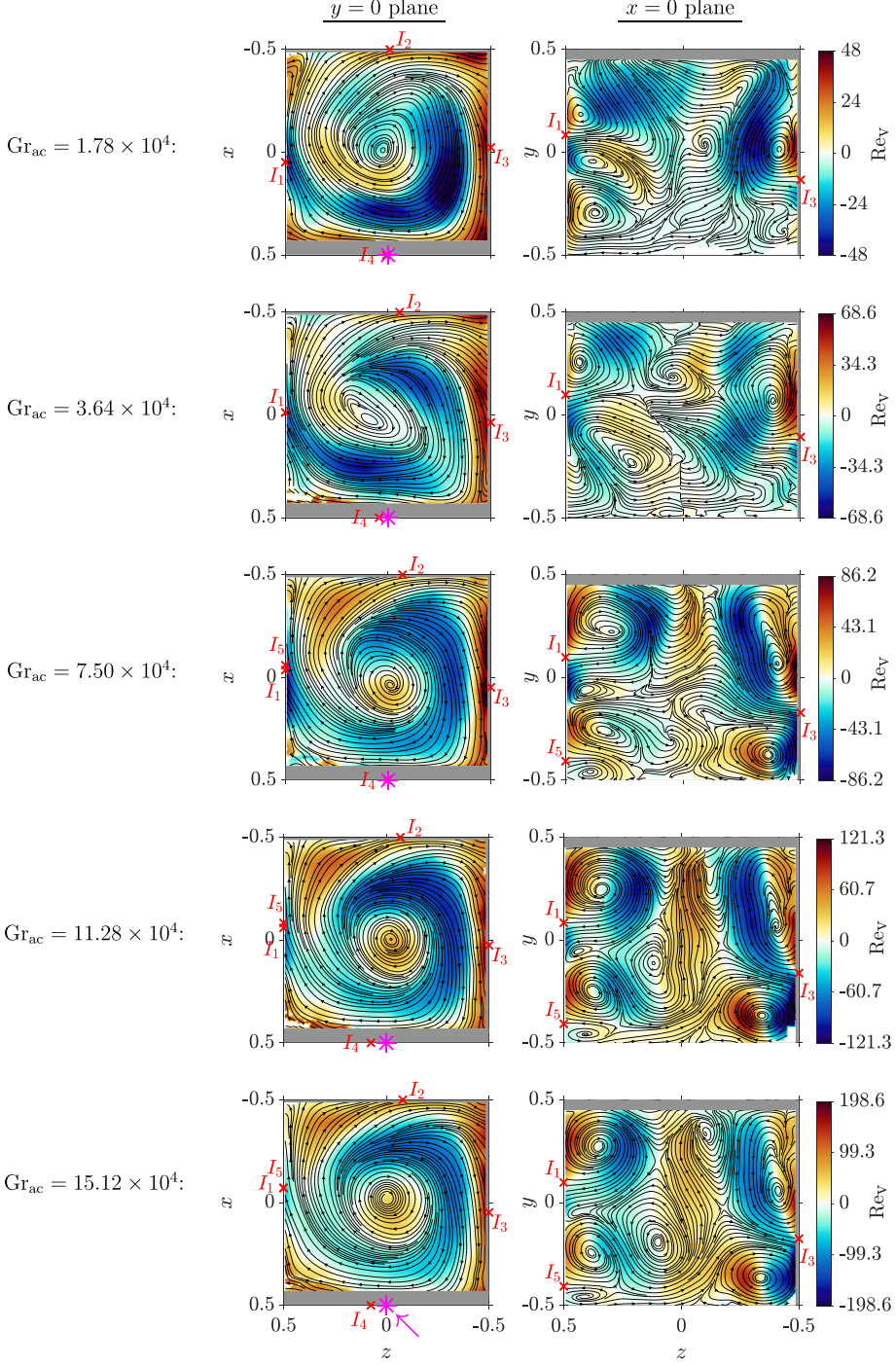


FIG. 6. Horizontal ($y = 0$, left) and vertical ($x = 0$, right) slices of the time-averaged vertical velocity component Re_v and streamlines of the projected velocity field for different values of Gr_{ac} . The purple star and arrow indicate the entry point of acoustic beam in the VOI and its orientation, respectively. Red "x" symbols labeled I_i are the locations where the i th jet axis impinges the walls. Figures on a same row share the same color levels. Gray areas indicate the location of noisy data.

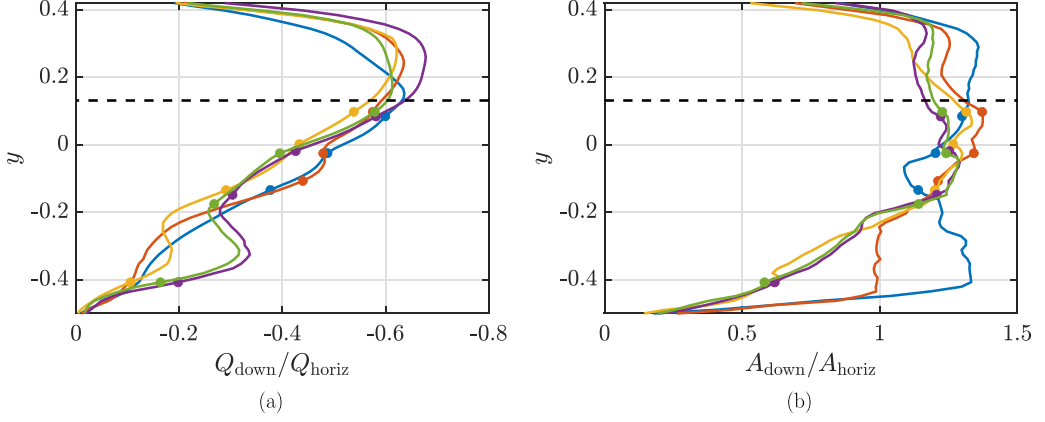


FIG. 7. (a) Vertical profiles of the ratio between the downward and horizontal flow rates $Q_{\text{down}}/Q_{\text{horiz}}$ (with $Q_{\text{horiz}} = \langle \bar{u}_\theta \rangle_{r,\theta,y} HL/2$). The profiles, obtained using Eq. (10), are shown for $\text{Gr}_{\text{ac}} = 1.78 \times 10^4$ (blue), $\text{Gr}_{\text{ac}} = 3.64 \times 10^4$ (orange), $\text{Gr}_{\text{ac}} = 7.50 \times 10^4$ (yellow), $\text{Gr}_{\text{ac}} = 11.28 \times 10^4$ (purple), and $\text{Gr}_{\text{ac}} = 15.12 \times 10^4$ (green). The x axis is reversed and that Q_{down} is counted negatively for downward motion. (b) Dimensionless cross-sectional area of downward-moving fluid A_{down} . The black dashed line locates the height at which the acoustic beam enters the cavity. The dots indicate the vertical positions of impingements of jets 1, 2, 3, and 5 in descending values of y , respectively.

velocity. The associated flow rate Q_{down} and the areas A_{down} of these surfaces are defined as

$$Q_{\text{down}}(y) = \sum_{\substack{n=1, \\ \bar{v}_n(y) < 0}}^{N_{\text{down}}} \bar{v}_n(y) \Delta x^2, \quad (10)$$

$$A_{\text{down}}(y) = N_{\text{down}} \Delta x^2.$$

In Eq. (10), the sum applies to the N_{down} points for which $\bar{v}_n = \bar{\mathbf{u}} \cdot \mathbf{e}_y < 0$ in a constant- y plane. Figure 7(a) shows the vertical distribution of Q_{down} for all forcing magnitudes. These profiles are normalized by the horizontal flow rate Q_{horiz} , which is based on $\langle \bar{u}_\theta \rangle_{r,\theta,y}$ and on the area $A_{\text{horiz}} = HL/2$. The downward flow rate increases from zero at the bottom wall to a maximum at a height that is similar to the entrance height of the beam. The maximum of Q_{down} ranges between $0.6 Q_{\text{horiz}}$ and $0.65 Q_{\text{horiz}}$ for all Gr_{ac} , i.e., the magnitude of the swirl motion dominates the magnitude of the downward flow. At greater y , Q_{down} decreases until vanishing completely at the free surface. Although this trend is reported for all Gr_{ac} , a “bump” of Q_{down} at $y \approx -0.31$ is visible only for $\text{Gr}_{\text{ac}} \geq 11.28 \times 10^4$. This feature is clearly not associated with a sudden change of A_{down} , since A_{down} is rather homogeneous over the entire cavity height [Fig. 7(b)]. Instead, this “bump” is caused by the J-shaped vortical structure near the bottom wall. This vortex creates local regions of important velocity and is sufficiently elongated to significantly increase Q_{down} there. Finally, the profiles of $Q_{\text{down}}/Q_{\text{horiz}}$ nearly collapse on a single curve. This provides evidence that Q_{down} nearly scales as $\sqrt{\text{Gr}_{\text{ac}}}$, since Q_{horiz} derives from a velocity showing a similar scaling [Eq. (9)].

Because of mass conservation, any downward flow is necessarily accompanied by ascending motions. These motions are mostly reported in two regions. First, along the walls, including in the corners of the VOI. Ascending flows occur there for all Gr_{ac} , and are essentially associated with the vortices arising from the vertical spreading of the jets at their impingements (right panel of Fig. 6). Second, in the central chimney visible only $\text{Gr}_{\text{ac}} > 7.50 \times 10^4$. This structure may span almost the entire cavity height for $\text{Gr}_{\text{ac}} \geq 11.28 \times 10^4$ and appears in a constant- y plane as a closed contour of positive vertical velocity at the center of the plane. The area of that closed contour shall be referred to as A_{chimney} . The rate of fluid Q_{chimney} flowing through A_{chimney} is then computed similarly to Q_{down}

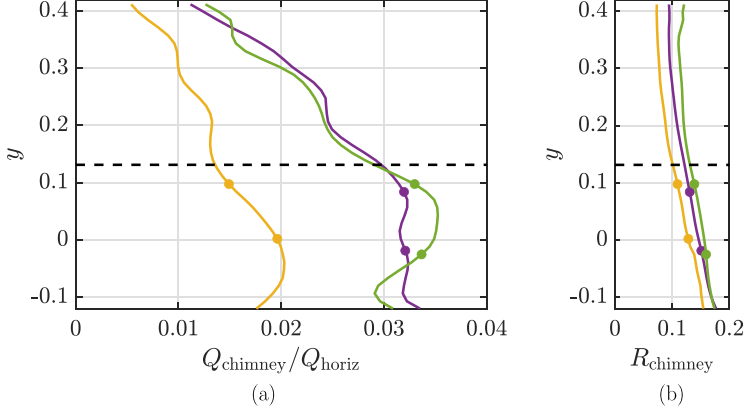


FIG. 8. (a) Vertical profiles of the normalized flow rate in the central chimney Q_{chimney} . The quantity used to normalized is $Q_{\text{horiz}} = \langle \bar{u}_\theta \rangle_{r,\theta,y} HL/2$. (b) Dimensionless chimney radius $R_{\text{chimney}} \approx \frac{\sqrt{A_{\text{chimney}}/\pi}}{L}$. The profiles are shown for $\text{Gr}_{\text{ac}} = 7.50 \times 10^4$ ($P_{\text{elec}} = 4$ W) in yellow, 11.28×10^4 (6 W) in purple, and 15.12×10^4 (8 W) in green. The black dashed line locates the height at which the beam enters the VOI. The dots indicate the vertical positions of the impingements of jets 1 (upper dots) and 2 (lower dots).

[Eq. (10)]; the only difference being that only the points for which $\bar{v}_n(y) > 0$ in the chimney are of interest.

Vertical profiles of $Q_{\text{chimney}}/Q_{\text{horiz}}$ are shown in Fig. 8(a) for $\text{Gr}_{\text{ac}} \geq 7.50 \times 10^4$. From the bottom of the cavity to $y \approx 0.13$, Q_{chimney} oscillates before steeply decreasing at heights corresponding to the forcing-free region. Just as Q_{down} , the ascending flow rate in the chimney seems to scale approximately as $\sqrt{\text{Gr}_{\text{ac}}}$ for $\text{Gr}_{\text{ac}} \geq 11.28 \times 10^4$. In addition, the overall increase of Q_{chimney} with the forcing causes the chimney structure to become slightly wider [Fig. 8(b)]. The radius R_{chimney} of the chimney is greater at the bottom of the VOI where it is fed with fluid and becomes thinner at higher y (above the dashed line in figures). The slope of each R_{chimney} profiles clearly changes once the force-free part of the VOI is reached, where R_{chimney} is typically 1/10th of the cavity size. Nevertheless, at a given Gr_{ac} , the maximum of Q_{chimney} is at most 6% of the largest $|Q_{\text{down}}|$. The vertical flow through the chimney thus only constitutes a small fraction of the total ascending motions. This result could not be predicted beforehand and is key to us: It means that the dominant upward motions occur near the walls and at the corners of the VOI with a flow rate $Q_{\text{up}} = -Q_{\text{down}} - Q_{\text{chimney}} \sim -Q_{\text{down}}$. This key feature confirms the expected efficiency of this configuration to mix the fluid outside the forcing region.

A complete picture of the helical flow can finally be drawn (Fig. 9). One can identify three distinct contributions to the overall helical flow, each being characterized by different ranges of their associated Reynolds number Re . The jets, for which Re is measured at the half distance between two consecutive beam reflections, constitute the primary flow: Their velocity magnitudes are the largest ones encountered in the fluid volume. The profiles of the mean jet velocities confirm a scaling as $\sqrt{\text{Gr}_{\text{ac}}}$ in the form of Eq. (3), except at the lowest forcing where they do not perfectly fit within the envelope. Having a Reynolds number several times smaller than those of the jets for each forcing, the overall fluid rotation driven by the jets can be seen as a secondary motion in the global flow. It nevertheless dominates, in terms of measured Reynolds numbers, the observed vertical flows, for which a single value of mean velocity $\langle U \rangle_y = \frac{1}{h} \int_h \frac{Q(y)}{A(y)} dy$ (h is the height over which the data for the vertical flow rates is available) is determined for each of the identified global vertical motions. In these even weaker flows, the slowest ones are encountered in the central chimney.

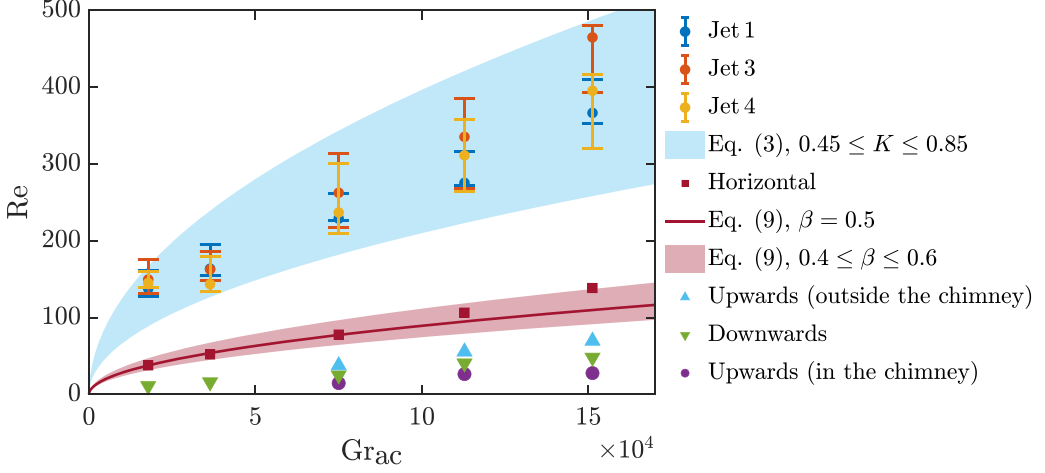


FIG. 9. Evolution with Gr_{ac} of the Reynolds numbers (based on D_s) associated with the different motions observed in the time-averaged flows. The Reynolds numbers of jets 1, 3, and 4 are measured at $x' = L_{jet}/(2D_s) = 2.2$, where L_{jet} is the distance between two consecutive acoustic reflection points and are bounded by measurements at $L_{jet}/(4D_s)$ and $3L_{jet}/(4D_s)$. The blue envelope is obtained for $x' = 2.2$. Equation (9) is plotted for $H = 160$ mm, $L = 183$ mm, $\delta = 15$ mm, $K = 0.65$, and $x' = 2.2$. Reynolds numbers based on the vertical flow rates of positive or negative velocity averaged over the vertical coordinates y (upward in the central chimney, downward and upward outside the central region, deduced with mass conservation equation) are also reported.

V. NEAR-IMPINGEMENT FLOW: MEAN STRUCTURE AND DYNAMICS

Finally, since the principle we rely on to generate a forcing with complex geometry is to use the reflection of the acoustic beam against the vessel wall, the regions around these reflections, where the jets impinge the wall, are key features of this flow. We shall examine them in more details using a second light setup (right column in Table I), especially focusing on the region where the first jet impingement occurs (green-shaded volume in Fig. 1).

The local time-averaged flow structure near I_1 is shown in Fig. 10 for $Gr_{ac} = 13.80 \times 10^4$ ($P_{elec} = 8$ W). The axes of the vortical structures have been determined using critical point theory: The measurement volume has been sliced in each direction and points of zero planar velocity have been sought [55]. The focii detected in constant- x planes (blue filament in Fig. 10) correspond to the axis of the roll resulting from the vertical spreading of jet 1 below I_1 and which is stretched by the overall rotating fluid motion. This structure is observed at lower values of Gr_{ac} as well (not shown). However, due to the small size of the measurement volume in the z direction, the axis of this structure could only be partially recovered for these forcing magnitudes. This nevertheless indicates that increasing the acoustic forcing confines this roll to the wall where impingement occurs. This, in turn, allows the central chimney to develop when the acoustic forcing is increased (Fig. 6). Although the measurement volume is too small in the y direction to detect the axis of the vortices located above I_1 and I_5 , the presence of these structures is inferred by the streamlines plotted in the $x = 0$ mm plane (Fig. 10). Another roll of nearly vertical axis is observed for $Gr_{ac} \geq 3.37 \times 10^4$ in the corner of the VOI as well (red filament in Fig. 10). One can also observe the presence of a third rotating structure in the mean flow near I_1 (black filament in Fig. 10). This roll swirls in constant- z planes and exists downstream I_1 for $Gr_{ac} \geq 3.37 \times 10^4$. As its axis points slightly towards the bottom of the fluid domain in the downstream direction, this structure might correspond to the upstream end of the vortex resulting from the impingement of jet 2 and located below I_2 . A greater size of the measurement domain in the z direction would be necessary to determine whether it is the case. Nevertheless, as we will see in this section, this rotating structure fluctuates significantly.

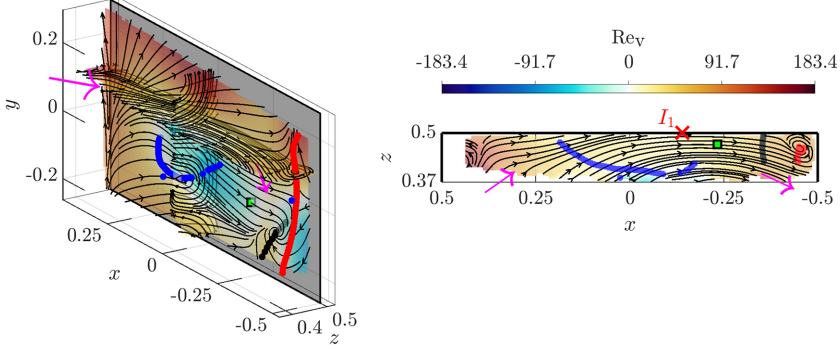


FIG. 10. Time-averaged flow structure near the first jet impingement I_1 ($\text{Gr}_{\text{ac}} = 13.80 \times 10^4$) with streamlines and slices of the vertical velocity component: isometric (left) and top (right) views. Colored spheres locate the focii (i.e., points of zero in-plane velocity and around which streamlines display a spiralling pattern) in several planes: constant- x (blue), constant- y (red), and constant- z (black) planes. Time-averaged inflow and outflow directions are identified by the purple arrows. The green square at $(x, y, z) = (-0.233, 0.053, 0.470)$ locates the point where the local dynamics are studied. The gray rectangle and thick black lines locate the solid vertical walls. Positive vertical velocity refers to upwards fluid motion, and both figures share same color levels.

The overall flow unsteadiness near I_1 may be witnessed through the temporal evolution of the total kinetic energy of the fluctuations:

$$e'_k(t) = \frac{1}{N_p(t)} \sum_{n=1}^{N_p(t)} \frac{1}{2} \mathbf{u}'(\mathbf{x}_n, t) \cdot \mathbf{u}'(\mathbf{x}_n, t), \quad (11)$$

where \mathbf{x}_n refers to the coordinates of the n th grid point in the discretized measurement domain, $\mathbf{u}'(\mathbf{x}_n, t) = \mathbf{u}(\mathbf{x}_n, t) - \bar{\mathbf{u}}(\mathbf{x}_n)$, and N_p is the total number of grid points. The overall level of e'_k , shown in Fig. 11, clearly increases with Gr_{ac} . Furthermore, the temporal evolution of e'_k features stronger fluctuations when acoustic forcing is enhanced and even displays isolated sharp peaks. These short and high-intensity events are particularly visible for $\text{Gr}_{\text{ac}} \geq 6.82 \times 10^4$ (Fig. 11). None of the observed signals are actually periodic over the recording duration, and for $\text{Gr}_{\text{ac}} = 13.8 \times 10^4$, for

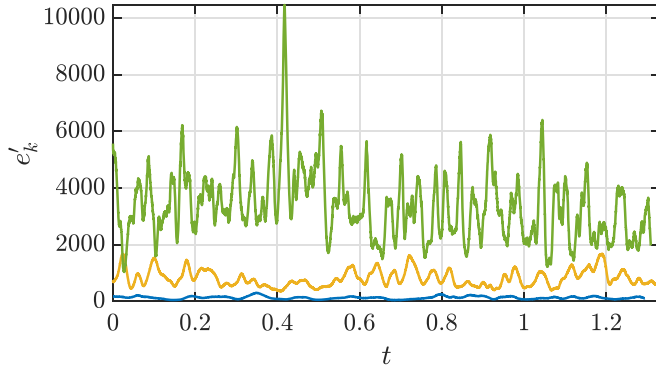


FIG. 11. Temporal evolution of the space-averaged kinetic energy of fluctuations, e'_k , as defined by Eq. (11) for $\text{Gr}_{\text{ac}} = 1.65 \times 10^4$ ($P_{\text{elec}} = 1$ W) (blue), $\text{Gr}_{\text{ac}} = 6.82 \times 10^4$ (4 W) (yellow), and $\text{Gr}_{\text{ac}} = 13.80 \times 10^4$ (8 W) (green).

instance, the short and high-intensity events are superimposed over significantly slower fluctuations. Unfortunately, the time series are too short to clearly identify leading frequencies in the spectrum of these signals; the associated dynamics would require significantly longer measurements to be thoroughly characterized. This situation has already been encountered during the investigation of a similar configuration [38], for which it has been shown that hours of observation were required to be able to characterize the flow dynamics [39]. Such recording durations are out of reach of our experiment.

This rise of unsteadiness with the forcing magnitude can also be observed locally through the strong deformations of the streamlines near I_1 . Their behavior is assessed by means of the angle θ between $\mathbf{u}(t)$ and $\bar{\mathbf{u}}$ at a given grid point $[(x, y, z) = (-0.233, 0.053, 0.470)]$, represented by a green square in Fig. 10. This quantity, as well as its root mean square, are defined as

$$\theta(t) = \arccos \left[\frac{\bar{\mathbf{u}} \cdot \mathbf{u}(t)}{\|\bar{\mathbf{u}}\| \|\mathbf{u}(t)\|} \right],$$

$$\theta_{\text{RMS}} = \sqrt{\frac{1}{N_s} \sum_{n=1}^{N_s} \theta(t_n)^2}, \quad (12)$$

where N_s refers to the number of snapshots. Note that both $\bar{\mathbf{u}}$ and $\mathbf{u}(t)$ are three dimensional in Eq. (12). The temporal evolution of θ is shown in Fig. 12 for both extreme values of power considered in this work. For $\text{Gr}_{\text{ac}} = 1.65 \times 10^4$, θ displays isolated fluctuations of large amplitude. For this acoustic forcing, the mean streamlines indicate that, at the probe location, the fluid flows mostly upwards. The peaks observed in the time series of θ for $\text{Gr}_{\text{ac}} = 1.65 \times 10^4$ hence correspond to short events during which, at this location in the VOI, the fluid abruptly starts to flow downwards before returning back to the local mean flow direction [Figs. 12(a) and 12(b)]. When the forcing is further enhanced, more peaks are observed. Such events, however, correspond to a different phenomenon than the one observed for $\text{Gr}_{\text{ac}} = 1.65 \times 10^4$. Contrarily to the lowest-forcing case, the mean streamlines are nearly horizontal at the probe location (Fig. 10). The large and short variations of θ observed in its time series for $\text{Gr}_{\text{ac}} = 13.80 \times 10^4$ in Fig. 12 are due to the emergence of a vortex, similarly to the one identified by the black filament in the time-averaged velocity field near the impingement I_1 (Figs. 10). This vortex, which enters the measurement domain from below when θ is low [Fig. 12(d)], moves upwards, causing a strong variation of θ as it passes close to the probe, and is then advected away (see the movie for $\text{Gr}_{\text{ac}} = 13.80 \times 10^4$ [56]). These rotating structures are observed several times in constant- z planes near the first impingement for a given recording and for $\text{Gr}_{\text{ac}} \geq 3.37 \times 10^4$.

These rolls (which are rotating about the z axis in the counterclockwise direction according to the point of view adopted in Fig. 12) have been tracked in time for each value of Gr_{ac} by locating the focii in constant- z planes at each time step, as it was done previously for the time-averaged flow. As shown in Fig. 13(a), these structures become more numerous when the forcing is increased, and their number N_v displays a linear evolution with Gr_{ac} . Only the case of $\text{Gr}_{\text{ac}} = 1.65 \times 10^4$ does not follow that trend: This behavior may be due to a too-short recording duration to be truthfully representative of the dynamics for that forcing.

Besides, by detecting when vortex core lines emerge and disappear from the measurement volume, one is able to recover the mean residence time $\langle t_r \rangle$ and vortex emergence frequency $\langle f \rangle$ associated with these structures, defined as

$$\langle t_r \rangle = \frac{1}{N_v} \sum_{n=1}^{N_v} (t_{\text{out}}^n - t_{\text{in}}^n), \quad (13)$$

$$\frac{1}{\langle f \rangle} = \langle T_e \rangle = \frac{1}{N_v - 1} \sum_{n=1}^{N_v-1} (t_{\text{in}}^{n+1} - t_{\text{in}}^n), \quad (14)$$

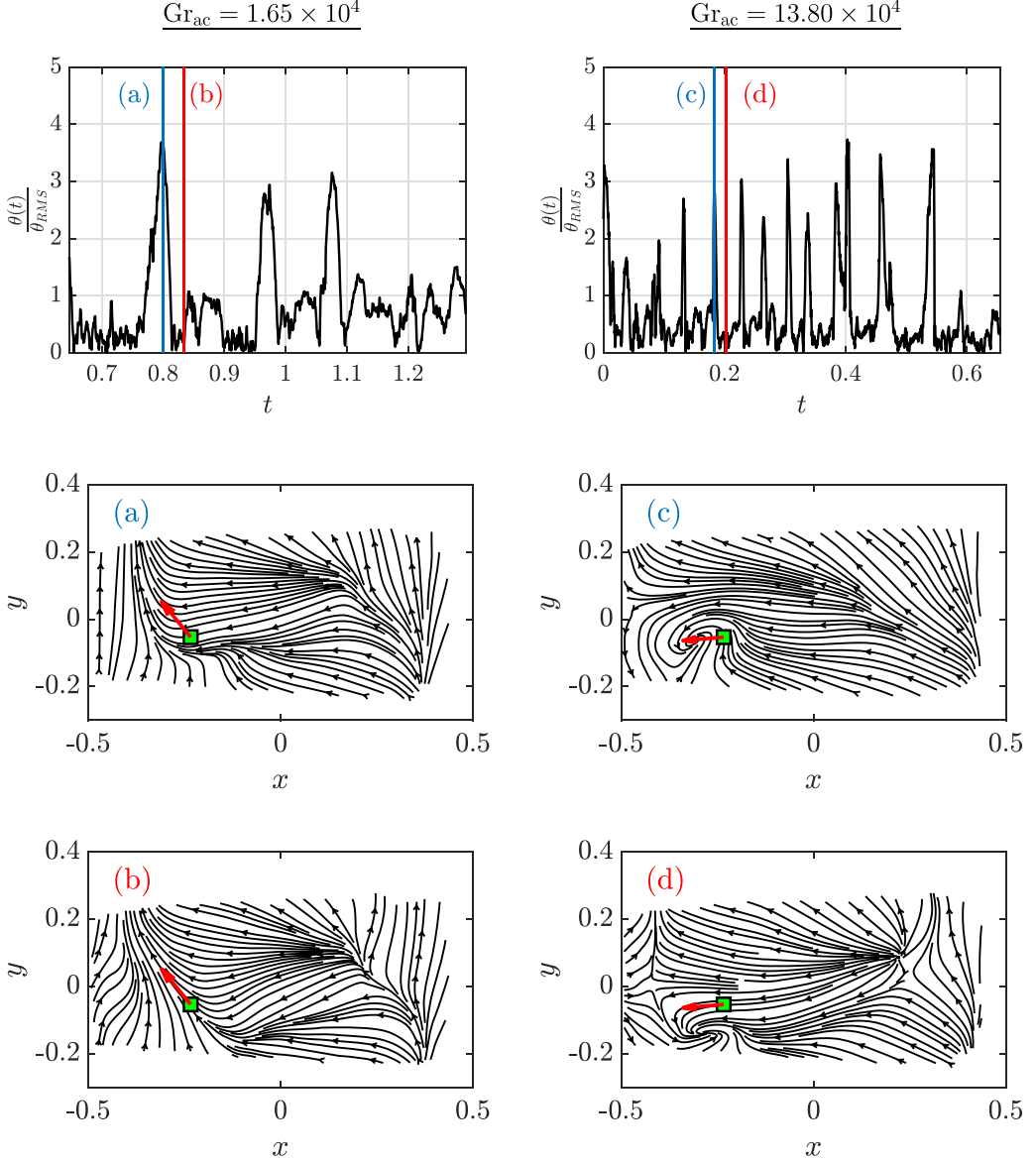


FIG. 12. Temporal evolution of θ (top plots), defined as the local angle between the instantaneous and time-averaged velocity computed using Eq. (12) and instantaneous streamlines in the vertical $z = 0.47$ plane for $Gr_{ac} = 1.65 \times 10^4$ (left) and 13.80×10^4 (right). The snapshots are extracted at the time stamps identified by the labeled vertical lines in the two upper graphs. The angle θ is normalized by its RMS value computed over the entire time series (20 min). The green square at $(x, y, z) = (-0.233, 0.053, 0.470)$ in the vertical slices indicates the probe location where θ is measured. The red arrow represents the projection in the vertical slice of the mean velocity vector measured at the probe.

where t_{in}^n and t_{out}^n are the timestamps at which the n th vortex core line enters and leaves the measurement volume, respectively, and $\langle T_e \rangle$ is the mean vortex emergence period. All the times are normalized by a characteristic diffusive time D_s^2/ν .

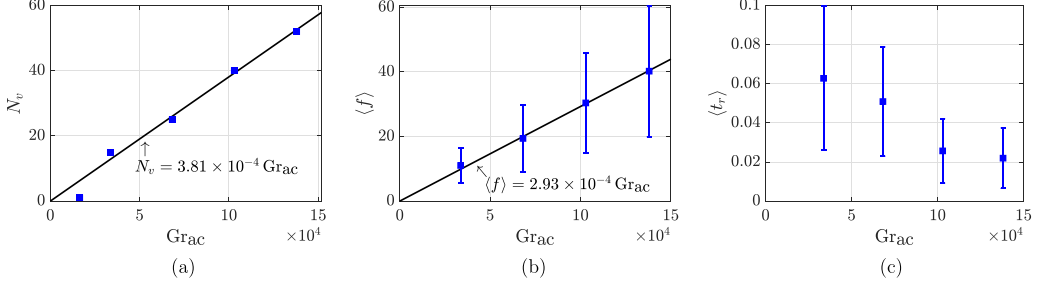


FIG. 13. Evolution with power of the statistics of the vortices rotating in the positive direction about the z axis in the vicinity of I_1 over the recording duration (20 min). (a) Number of tracked vortices. (b) Mean emergence frequency $\langle f \rangle$, defined by Eq. (14). (c) Dimensionless mean residence time $\langle t_r \rangle$ of these vortices in the volume. Values of $\langle f \rangle$ are bounded using Eq. (15) and those of $\langle t_r \rangle$ by their standard deviation. The characteristic diffusive time D_s^2/ν is used to make frequency and residence time dimensionless.

From Eq. (14), $\langle f \rangle$ can be bounded by

$$\Delta f = \langle f \rangle \frac{\sigma_{T_e}}{\langle T_e \rangle}, \quad (15)$$

where σ_{T_e} stands for the standard deviation of T_e determined for each value of Gr_{ac} . The evolution with power of the frequency and the mean residence times are shown in Figs. 13(b) and 13(c), respectively. Both quantities logically appear to be faster than the diffusion time at the scale of the acoustic source. Frequency increases linearly with acoustic forcing (however, with a greater dispersion), meaning that no change of flow regime seems to occur in the range of investigated acoustic forcing. On the other hand, $\langle t_r \rangle$ decreases with Gr_{ac} and more significantly at low than at high Gr_{ac} . Nevertheless, the observed drop of this quantity with Gr_{ac} indicates that, although they emerge at a higher rate, vortices are rapidly swept away from the measurement domain when the forcing magnitude increases. In other words, the helical flow driven by ultrasounds is far from being steady, and its unsteadiness significantly intensifies when the acoustic forcing magnitude is increased.

VI. CONCLUSION

An experimental study of an acoustic streaming flow inside a water-filled cuboid cavity has been presented. Such flow results from an energy transfer mechanism: the viscosity-induced dissipation occurring in the bulk of the fluid converts the acoustic energy into mechanical energy. The weakly invasive nature of this phenomenon makes acoustic streaming a viable alternative to more traditional ways of putting the fluid into motion (e.g., using a propeller), which may be inappropriate due to tight packaging constraints or to the properties of the fluids to be stirred, for instance.

The investigated flow is driven by an ultrasonic beam (2 MHz) radiated by a plane circular transducer of 30 mm in diameter. It enters a quasicubic water-filled aquarium made of glass in the upper part of a lateral, vertical wall. The acoustic beam is given initial inclinations of 45° and 8° in the horizontal and vertical planes, respectively, forcing it to perfectly reflect on each vertical boundary at its middle vertical line, while at the same time to travel downwards the fluid volume. The path followed by the acoustic beam is made of five reflections before reaching the bottom of the aquarium, where the sound waves are absorbed. On the contrary, the upper surface is left free. The acoustic field then exhibits a helix-shaped structure, resulting in a complex three-dimensional flow. The corresponding velocity field is measured in the entire fluid domain by means of particle tracking velocimetry (PTV) for different forcing magnitudes, controlled by the electrical power supplied to the acoustic source. The magnitude of the forcing is described by a dimensionless quantity called acoustic Grashof number.

The time-averaged flow is made of several jets roughly following the acoustic beam and flowing towards the bottom of the fluid volume. The velocity within each of these jets follows reasonably well the scaling law of an individual free jet that would originate from the point of reflection given by Eq. (3): $Re_{jet} \approx K \sqrt{Gr'_{ac} x'}$. This scaling law offers a useful tool for the prediction of flows driven by acoustic beams reflecting on solid boundaries that may be used in specific applications. These jets create a swirl at the scale of the entire cavity, about a vertical axis approximately located at the center of the cavity. Its intensity varies linearly with that of the jets but remains considerably smaller by a factor controlled by the ratio of the thickness of the wall boundary layers near the jets and the size of the box. The jets split at the solid boundaries and this gives rise to vortices which are stretched by the large-scale rotation. An important feature of the large-scale flow structure is the return flow induced by the downward-pointing acoustic force. To this end, the flows in both vertical directions, as well as their dependence on the forcing magnitude, have been quantified as well: While downward motion mostly occurs in the surroundings of the jets, the fluid essentially flows upwards close to the solid boundaries where jet impingements occur, as well as in the center of the cavity. The latter region of ascending fluid, similarly to a chimney, becomes particularly visible for $Gr_{ac} \geq 7.50 \times 10^4$ ($P_{elec} \geq 4$ W). However, the rate of fluid flowing through the chimney is an order of magnitude lower than the one of ascending mass of fluid near the vertical walls. This property may be very useful in mixing applications where stagnations regions, which tend to form in the vicinity of boundaries, need to be avoided. Nevertheless, given the change in intensity of the return flow with acoustic power, our study raises the questions of whether a much stronger return flow could be obtained either at the center or near the walls by adjusting both acoustic and geometric parameters like the pitch of the helical forcing resulting from the vertical tilting of the acoustic source.

The unsteady properties of the flow were studied locally only. Due to the limitations of time-resolved PTV in terms of volume of investigation, we restricted our analysis to the critical near-wall region where the jets impingements occurs and in particular, the first impingement. Aperiodic fluctuations of small amplitudes observed at the lowest acoustic forcing magnitude are amplified when the acoustic power is increased, up to the point where short and intense momentum bursts are witnessed for the highest forcing. These high-intensity events involve the emergence and advection of vortical structures near the impingement of the first jet, and their origin may be closely related to strong interactions with the fifth jet, which impinges the same surface at a lower height. Although these structures do not appear periodically, their frequency of emergence (defined as the inverse of the mean time difference between the emergence of two consecutive vortices) follows a linear dependence on the power injected into the fluid domain, indicating a smooth evolution of the flow structure rather than an abrupt change of the flow regime. This linear increase of the vortex emergence rate is accompanied by a decrease of their residence time in the volume encompassing the first jet impingement, a consequence of the rise of an overall convective motion in the entire fluid volume when the forcing is enhanced. While this tendency does not give an indication of how the flow evolves toward chaos and turbulence, it offers a measure of unsteadiness and a prediction of the dominant flow frequencies that may be exploited to fine-tune heat and mass transport in specific applications. Just like the average return flow, it remains to be understood how these properties are affected by acoustic and geometric parameters.

In the end, this study shows that multiple reflections of a single monochromatic ultrasonic beam on the boundaries of a fluid container can give rise to a large and complex three-dimensional flow. This is not only interesting for regular stirring applications, but it is also relevant for industrial processes, such as solidification of metal alloys and semiconductors, in which the access to melts is highly constrained due to tight thermal insulation requirements. The implementation of this technique into these individual processes requires predictions that may be obtained from the observed scaling laws for the individual jet together with the scaling law of the global swirl we derived. The vertical flow, on the other hand, is harder to predict, both in shape and in intensity, but we showed that it increases with the forcing in a nontrivial way. More precise predictions both for

the return flow and the unsteady properties (main frequency, fluctuation energy and statistics) would require further work on their dependence on both geometric and acoustic parameters.

ACKNOWLEDGMENTS

The authors thank Cédric Marmounier and Nathalie Grosjean for technical assistance on the experimental setup as well as LaVision company for the software support. This work was carried out as part of the BRASSOA project supported by the Institut Carnot Ingénierie@Lyon. For the purpose of Open Access, a CC-BY public copyright licence has been applied by the authors to the present document and will be applied to all subsequent versions up to the Author Accepted Manuscript arising from this submission.

-
- [1] M. Faraday, On a peculiar class of acoustical figures; and on certain forms assumed by groups of particles upon vibrating elastic surfaces, *Philos. Trans. R. Soc. Lond.* **121**, 299 (1831).
 - [2] S. M. Hagsäter, T. Glasdam Jensen, H. Bruus, and J. P. Kutter, Acoustic resonances in microfluidic chips: Full-image micro-PIV experiments and numerical simulations, *Lab Chip* **7**, 1336 (2007).
 - [3] J. Friend and L. Y. Yeo, Microscale acoustofluidics: Microfluidics driven via acoustics and ultrasonics, *Rev. Mod. Phys.* **83**, 647 (2011).
 - [4] P. B. Muller and H. Bruus, Theoretical study of time-dependent, ultrasound-induced acoustic streaming in microchannels, *Phys. Rev. E* **92**, 063018 (2015).
 - [5] A. Green, J. S. Marshall, D. Ma, and J. Wu, Acoustic streaming and thermal instability of flow generated by ultrasound in a cylindrical container, *Phys. Fluids* **28**, 104105 (2016).
 - [6] M. Baudoin and J.-L. Thomas, Acoustic tweezers for particle and fluid micromanipulation. Annual review of fluid mechanics, *Annu. Rev. Fluid Mech.* **52**, 205 (2019).
 - [7] S. Cleve, M. Guédra, C. Mauger, C. Inserra, and P. Blanc-Benon, Microstreaming induced by acoustically trapped, non-spherically oscillating microbubbles, *J. Fluid Mech.* **875**, 597 (2019).
 - [8] A. A. Doinikov, G. Regnault, C. Mauger, P. Blanc-Benon, and C. Inserra, Acoustic microstreaming produced by two interacting gas bubbles undergoing axisymmetric shape oscillations, *J. Fluid Mech.* **931**, A19 (2022).
 - [9] M. Fauconnier, C. Mauger, J.-C. Béra, and C. Inserra, Nonspherical dynamics and microstreaming of a wall-attached microbubble, *J. Fluid Mech.* **935**, A22 (2022).
 - [10] J. Li, A. Crivoi, X. Peng, L. Shen, Y. Pu, Z. Fan, and S. A. Cummer, Three dimensional acoustic tweezers with vortex streaming, *Commun. Phys.* **4**, 113 (2021).
 - [11] C. Eckart, Vortices and streams caused by sound waves, *Phys. Rev.* **73**, 68 (1948).
 - [12] P. Westervelt, The theory of steady rotational flow generated by a sound field, *J. Acoust. Soc. Am.* **25**, 60 (1953).
 - [13] W. L. Nyborg, Acoustic streaming due to attenuated plane waves, *J. Acoust. Soc. Am.* **25**, 68 (1953).
 - [14] J. Lighthill, Acoustic streaming, *J. Sound Vib.* **61**, 391 (1978).
 - [15] J. S. Marshall and J. Wu, Acoustic streaming, fluid mixing, and particle transport by a gaussian ultrasound beam in a cylindrical container, *Phys. Fluids* **27**, 103601 (2015).
 - [16] S. Miralles, M. Albaric, V. Brizé, P. Guy, B. Vincent, J.-P. Garandet, J.-C. Willemetz, D. Henry, and V. Botton, In situ ultrasonic interface tracking for photovoltaic silicon directional solidification, *J. Cryst. Growth* **621**, 127362 (2023).
 - [17] W. Dridi, D. Henry, and H. Ben Hadid, Influence of acoustic streaming on the stability of melt flows in horizontal bridgman configurations, *J. Cryst. Growth* **310**, 1546 (2008).
 - [18] M.-C. Charrier-Mojtabi, A. Fontaine, and A. Mojtabi, Influence of acoustic streaming on thermo-diffusion in a binary mixture under microgravity, *Int. J. Heat Mass Transf.* **55**, 5992 (2012).
 - [19] O. Bulliard-Sauret, J. Berindei, S. Ferrouillat, L. Vignal, A. Momponteil, C. Poncet, J.-M. Leveque, and N.

- Gondrexon, Heat transfer intensification by low or high frequency ultrasound: Thermal and hydrodynamic phenomenological analysis, *Exp. Therm. Fluid Sci.* **104**, 258 (2019).
- [20] M.-C. Charrier-Mojtabi, X. Jacob, T. Dochy, and A. Mojtabi, Species separation of a binary mixture under acoustic streaming, *Eur. Phys. J. E* **42**, 64 (2019).
- [21] G. S. Lebon, G. Salloum-Abou-Jaoude, D. Eskin, I. Tzanakis, K. Pericleous, and P. Jarry, Numerical modelling of acoustic streaming during the ultrasonic melt treatment of direct-chill (DC) casting, *Ultrason. Sonochem.* **54**, 171 (2019).
- [22] N. El Ghani, S. Miralles, V. Botton, D. Henry, H. Ben Hadid, B. Ter-Ovanessian, and S. Marcelin, Acoustic streaming enhanced mass transfer at a wall, *Int. J. Heat Mass Transf.* **172**, 121090 (2021).
- [23] S. Dumitrica, D. Vizman, J.-P. Garandet, and A. Popescu, Numerical studies on a type of mechanical stirring in directional solidification method of multicrystalline silicon for photovoltaic applications, *J. Cryst. Growth* **360**, 76 (2012).
- [24] M. Chatelain, V. Botton, M. Albaric, D. Pelletier, B. Cariteau, D. Abdo, and M. Borrelli, Mechanical stirring influence on solute segregation during plane front directional solidification, *Int. J. Therm. Sci.* **126**, 252 (2018).
- [25] Y. Delannoy, Purification of silicon for photovoltaic applications, *J. Cryst. Growth* **360**, 61 (2012).
- [26] O. Pätzold, K. Niemietz, R. Lantzsche, V. Galindo, I. Grants, M. Bellmann, and G. Gerbeth, The use of magnetic fields in vertical bridgman/gradient freeze-type crystal growth, *Eur. Phys. J.: Spec. Top.* **220**, 243 (2013).
- [27] M. Cablea, K. Zaidat, A. Gagnoud, A. Nouri, and Y. Delannoy, Directional solidification of silicon under the influence of travelling magnetic field, *J. Cryst. Growth* **401**, 883 (2014).
- [28] M. Cablea, K. Zaidat, A. Gagnoud, A. Nouri, G. Chichignoud, and Y. Delannoy, Multi-crystalline silicon solidification under controlled forced convection, *J. Cryst. Growth* **417**, 44 (2015).
- [29] W. Dridi, D. Henry, and H. Ben Hadid, Influence of acoustic streaming on the stability of a laterally heated three-dimensional cavity, *Phys. Rev. E* **77**, 046311 (2008).
- [30] T. P. Lyubimova and R. V. Skuridin, The effect of acoustic wave on the stability of stationary convective flow of binary fluid in a horizontal layer subjected to horizontal temperature and concentration gradients, *Int. J. Heat Mass Transf.* **132**, 789 (2019).
- [31] G. S. B. Lebon, I. Tzanakis, K. Pericleous, D. Eskin, and P. S. Grant, Ultrasonic liquid metal processing: The essential role of cavitation bubbles in controlling acoustic streaming, *Ultrason. Sonochem.* **55**, 243 (2019).
- [32] S. Absar, P. Pasumarthi, and H. Choi, Numerical and experimental studies about the effect of acoustic streaming on ultrasonic processing of metal matrix nanocomposites (MMNCs), *J. Manufact. Process.* **28**, 515 (2017).
- [33] M. C. Schenker, M. J. Pourquié, D. G. Eskin, and B. J. Boersma, Piv quantification of the flow induced by an ultrasonic horn and numerical modeling of the flow and related processing times, *Ultrason. Sonochem.* **20**, 502 (2013).
- [34] T. Kamakura, T. Sudo, K. Matsuda, and Y. Kumamoto, Time evolution of acoustic streaming from a planar ultrasound source, *J. Acoust. Soc. Am.* **100**, 132 (1996).
- [35] H. Mitome, The mechanism of generation of acoustic streaming, *Electron. Commun. Jpn.* **81**, 1 (1998).
- [36] B. Moudjed, V. Botton, D. Henry, H. Ben Hadid, and J.-P. Garandet, Scaling and dimensional analysis of acoustic streaming jets, *Phys. Fluids* **26**, 093602 (2014).
- [37] B. Moudjed, V. Botton, D. Henry, S. Millet, and H. Ben Hadid, Y-shaped jets driven by an ultrasonic beam reflecting on a wall, *Ultrasonics* **68**, 33 (2016).
- [38] T. Cambonie, B. Moudjed, V. Botton, D. Henry, and H. Ben Hadid, From flying wheel to square flow: Dynamics of a flow driven by acoustic forcing, *Phys. Rev. Fluids* **2**, 123901 (2017).
- [39] G. Launay, T. Cambonie, D. Henry, A. Pothérat, and V. Botton, Transition to chaos in an acoustically driven cavity flow, *Phys. Rev. Fluids* **4**, 044401 (2019).
- [40] A. Riaud, M. Baudoin, O. Bou Matar, J.-L. Thomas, and P. Brunet, On the influence of viscosity and caustics on acoustic streaming in sessile droplets: An experimental and a numerical study with a cost-effective method, *J. Fluid Mech.* **821**, 384 (2017).

- [41] T. Dauxois, S. Joubaud, P. Odier, and A. Venaille, Instabilities of internal gravity wave beams, *Annu. Rev. Fluid Mech.* **50**, 131 (2018).
- [42] A. Y. Savchenko, N. V. Tabiryan, and B. Y. Zel'dovich, Transfer of momentum and torque from a light beam to a liquid, *Phys. Rev. E* **56**, 4773 (1997).
- [43] H. Chraïbi, R. Wunenburger, D. Lasseux, J. Petit, and J.-P. Delville, Eddies and interface deformations induced by optical streaming, *J. Fluid Mech.* **688**, 195 (2011).
- [44] Y. Wang, Q. Zhang, Z. Zhu, F. Lin, J. Deng, G. Ku, S. Dong, S. Song, M. K. Alam, D. Liu, Z. Wang, and J. Bao, Laser streaming: Turning a laser beam into a flow of liquid, *Sci. Adv.* **3**, e1700555 (2017).
- [45] B. Moudjed, V. Botton, D. Henry, S. Millet, J.-P. Garandet, and H. Ben Hadid, Near-field acoustic streaming jet, *Phys. Rev. E* **91**, 033011 (2015).
- [46] Precision Acoustics Ltd, AptFlex F28–Technical datasheet, <https://www.acoustics.co.uk/wp-content/uploads/2023/06/F28-TDS-V2-0423.pdf>.
- [47] D. Schanz, S. Gesemann, and A. Schröder, Shake-the-box: Lagrangian particle tracking at high particle image densities, *Exp. Fluids* **57**, 70 (2016).
- [48] R. Ben Haj Slama, B. Gilles, M. Ben Chiekh, and J.-C. Béra, Piv for the characterization of focused field induced acoustic streaming: seeding particle choice evaluation, *Ultrasonics* **76**, 217 (2017).
- [49] Rapport de mesure: Transducteur monoélément 2 MHz, IMASONIC SAS (2011).
- [50] I. Diner and C. Zamfirescu, *Drying Phenomena: Theory and Applications* (John Wiley & Sons, New York, 2015).
- [51] See Supplemental Material at <http://link.aps.org/supplemental/10.1103/PhysRevFluids.9.024101> for the time-averaged flow measured at maximum forcing, entitled “animated_isocontour_velocity_magnitude.mp4” for an animated representation of the velocity magnitude isocontour.
- [52] J. C. R. Hunt, A. A. Wray, and P. Moin, Eddies, stream and convergence zones in turbulent flows. Tech. rept. CTR-S88. Center Turbulence Research (1988).
- [53] P. Chakraborty, S. Balachandar, and R. J. Adrian, On the relationships between local vortex identification schemes, *J. Fluid Mech.* **535**, 189 (2005).
- [54] See Supplemental Material at <http://link.aps.org/supplemental/10.1103/PhysRevFluids.9.024101> for an animated representation of the Q -criterion isocontour for the time-averaged flow measured at maximum forcing, entitled “animated_isocontour_Q_criterion.mp4”.
- [55] M. S. Chong, A. E. Perry, and B. J. Cantwell, A general classification of three-dimensional flow fields, *Phys. Fluids* **2**, 765 (1990).
- [56] See Supplemental Material at <http://link.aps.org/supplemental/10.1103/PhysRevFluids.9.024101> for the movie of the instantaneous velocity field near the first jet impingement at maximum forcing, entitled “instantaneous_velocity_near_I1.mp4”.